Free induction decay caused by a dipole field

C. H. Ziener,[1,2] F. T. Kurz,[1,2] and T. Kampf[3]

[1]*German Cancer Research Center-DKFZ, Im Neuenheimer Feld 280, 69120 Heidelberg, Germany*

[2]*Heidelberg University, Department of Neuroradiology, Im Neuenheimer Feld 400, 69120 Heidelberg, Germany*

[3]*University of Würzburg, Department of Experimental Physics 5, Am Hubland, 97074 Würzburg, Germany*

(Received 24 July 2014; published 17 March 2015)

We analyze the free induction decay of nuclear spins under the influence of restricted diffusion in a magnetic dipole field around cylindrical objects. In contrast to previous publications no restrictions or simplifications concerning the diffusion process are made. By directly solving the Bloch-Torrey equation, analytical expressions for the magnetization are given in terms of an eigenfunction expansion. The field strength-dependent complex nature of the eigenvalue spectrum significantly influences the shape of the free induction decay. As the dipole field is the lowest order of the multipole expansion, the obtained results are important for understanding fundamental mechanisms of spin dephasing in many other applied fields of nuclear magnetic resonance such as biophysics or material science. The analytical methods are applied to interpret the spin dephasing in the free induction decay in cardiac muscle and skeletal muscle. A simple expression for the relevant transverse relaxation time is found in terms of the underlying microscopic parameters of the muscle tissue. The analytical results are in agreement with experimental data. These findings are important for the correct interpretation of magnetic resonance images for clinical diagnosis at all magnetic field strengths and therapy of cardiovascular diseases.

DOI: 10.1103/PhysRevE.91.032707 PACS number(s): 87.10.Ed, 87.64.kj, 87.61.Bj

I. INTRODUCTION

In nuclear magnetic resonance, the gradient echo technique is a powerful tool in imaging and the knowledge of the behavior of the free induction decay is mandatory for understanding and interpreting the measured signal. The free induction decay is mainly influenced by field inhomogeneities caused by the microscopic susceptibility differences inside the volume of interest. In biological tissues, these susceptibility differences are often generated by microscopic structures, e.g., the vascular network. The parameters of the microscopic structures are related to physiological and functional parameters, which therefore can be detected via nuclear magnetic resonance.

For example, the microscopic parameters of muscle tissue such as capillary radius or regional blood volume are of interest in the diagnosis of muscle diseases. Gradient echo-based magnetic resonance imaging allows us to analyze these parameters quantitatively and noninvasively. It uses the characteristic influence of these microscopic parameters on the free induction decay. Thus, the problem under consideration is to connect the acquired signal with the microscopic parameters that are not directly accessible due to the limited resolution of conventional magnetic resonance imaging.

The dephasing of spins in the local magnetic dipole field results in a faster free induction decay, as, for example, shown for myocardial tissue where the dipole fields are generated by blood-filled capillaries [1]. In this case the measured free induction decay depends on the microscopic parameters of the myocardial tissue, i.e., capillary diameter, volume fraction of the dipole field generating capillaries, and deoxyhemoglobin content, which correlates to the strength of the microscopic susceptibility difference between the dipole and the surrounding medium. Furthermore, due to the microscopic dimensions of the relevant structures, the diffusion process of the spins around the dipole fields has to be taken into account.

Different approaches to analyze the dephasing mechanisms in inhomogeneous fields have been developed. The static dephasing approach [2,3] can be used in the case of larger structures where the displacement of the diffusing spin during the observed time evolution is smaller than the size of the relevant structure. However, most structures of interest contain small structures, as, for example, biological tissues, which consist mainly of cells and vessels and the diffusion around them cannot be neglected. Bauer *et al*. developed a model to describe the transverse relaxation time by respecting the diffusion [1,4]. They adapted the strong collision approach [5] to analyze the diffusion process and applied the mean relaxation time approximation [6] to obtain the monoexponential transverse relaxation time T_2^*, which is an important parameter, as it is often not possible to acquire a fully spatially resolved free induction decay. In experiments, the transverse relaxation time is determined by fitting an exponential function to the signals obtained from gradient echo images. Recently, we developed the formalism of the local frequency density of states around field inhomogeneities to obtain the lineshape of the free induction decay directly [7]. Especially in the case of cylindrical field inhomogeneities that can be used as a model for the capillaries in the myocardium or skeletal muscle, we observed that the free induction decay is not purely monoexponential, but exhibits oscillating components of the signal decay under certain circumstances. To analyze theses circumstances, an analogy of the signal evolution to the damped driven harmonic oscillator can be given [8], which enables us to distinguish different dephasing regimes.

Nevertheless, it is important to mention that the solution of the Bloch-Torrey equation for the dephasing in the dipole field is of great interest in many fields of modern physics. The dipole field is the lowest order in the multipole expansion and, therefore, serves as a generic model to study principle effects. Furthermore, due to the purely imaginary potential, the Bloch-Torrey equation serves as a generic model for non-Hermitean quantum mechanics where full analytical solutions of the simple potentials are of great importance. The analytical solution exhibits typical properties known from

non-Hermitean quantum mechanics, e.g., complex eigenvalues and branching points. Hence, it is possible to describe the exact time evolution of the free induction decay, which extends the usually assumed exponential form.

Especially for medical applications, an accurate quantification of physiological parameters is highly important for clinical decision making and planning of therapy. Until now, all methods to describe the free induction decay in biological tissues are approximations of the real diffusion process. Therefore, it is necessary to determine a full analytical solution which is in agreement with experimental data, as presented in this work.

II. MICROSCOPIC STRUCTURE AND DEPHASING

In principle, the myocardium and also the skeletal muscle tissue can be considered as an arrangement of parallel capillaries whose alignment can be described by Krogh's capillary model [9]. As visualized in Fig. 1, each of these capillaries supplies a coaxial cylindrical volume with radius R_D in which the diffusion of the nuclear spins with diffusion coefficient D occurs.

Due to the external magnetic field B_0, each capillary generates a local Larmor frequency that has the form of a two-dimensional dipole field [10]:

$$\omega(r,\phi) = \delta\omega R_C^2 \frac{\cos(2\phi)}{r^2}, \tag{1}$$

with capillary radius R_C and frequency shift $\delta\omega$ on the capillary surface $\delta\omega = \omega(r = R_C,\phi = 0)$. The regional blood volume in the myocardial tissue is defined as

$$\eta = \frac{R_C^2}{R_D^2}. \tag{2}$$

Generally, the influence of neighboring capillaries is not negligible. However, Krogh's capillary model only considers single capillaries that cannot cover a space without overlapping. Therefore, we chose the dephasing volume in such a way that the volume fraction is preserved as demonstrated in Fig. 1. The supply area equals the area of the respective hexagon and, thus, the approximation used describes the real situation for small volume fractions. We assume a regular arrangement, i.e., in the cross-sectional view, the capillary is in the center of a hexagon and has six nearest neighbors. Each hexagon in Krogh's capillary model (see Fig. 1) with side length a and area $A = 3\sqrt{3}a^2/2$ is replaced by a circle with radius R_D and the same area $A = \pi R_D^2$. Therefore, the distance between two capillaries is $2a = 2R_D\sqrt{2\pi/[3\sqrt{3}]}$. The effects of neighboring capillaries can be neglected if the characteristic

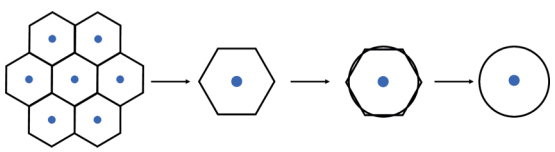

FIG. 1. (Color online) Regular arrangement of parallel capillaries in Krogh's capillary model and stepwise simplification to a single bloodfilled capillary [blue (gray) circle] with radius R_C, which is surrounded by the dephasing cylinder (black) with radius R_D.

frequency $\delta\omega$ at the surface of a capillary is much higher than the frequencies caused by the six surrounding capillaries with distance $2a$. Using Eq. (1), we obtain the inequality $\delta\omega \gg 6\delta\omega R_C^2/[2a]^2$, that leads to an estimation for the volume fraction: $\eta \ll 4\pi/[9\sqrt{3}] = 0.81$.

The dephasing of the local transverse magnetization $m(r,\phi,t)$ in the two-dimensional dipole field around a capillary is described by the Bloch-Torrey equation [11]:

$$\frac{\partial}{\partial t}m(r,\phi,t) = \left[D\Delta - i\omega(r,\phi) - \frac{1}{T_2}\right]m(r,\phi,t), \tag{3}$$

where T_2 is the intrinsic spin-spin relaxation time of the tissue surrounding the capillary. In the surrounding tissue inside the dephasing cylinder ($R_C \leqslant r \leqslant R_D$), the diffusion process with diffusion coefficient D occurs. In Krogh's capillary model reflecting boundary conditions are imposed on the surface of the capillary as well as the surface of the dephasing cylinder [12,13]:

$$\left.\frac{\partial}{\partial r}m(r,\phi,t)\right|_{r=R_C} = 0 = \left.\frac{\partial}{\partial r}m(r,\phi,t)\right|_{r=R_D}. \tag{4}$$

Initially, at $t = 0$ the local transverse magnetization $m(r,\phi,t) = m_0$ is generated by an excitation pulse and due to the dephasing and diffusion processes the local transverse magnetization $m(r,\phi,t)$ evolves in time and space, governed by the Bloch-Torrey equation with its respective boundary conditions. However, the resolution of a clinical MR-scanner does not allow to resolve $m(r,\phi,t)$ spatially. A typical imaging voxel is more than one order of magnitude larger than the dephasing volume of a single capillary. Therefore, the averaged signal over the dephasing volume

$$S(t) = \int_0^{2\pi}\int_{R_C}^{R_D} m(r,\phi,t) r\, dr d\phi \tag{5}$$

is measured. In the following we will obtain explicit expressions for the total signal in dependence of the underlying tissue parameters.

III. SIGNAL FORMATION

The total signal that can be measured depends on the microscopic tissue parameters of the myocardium that determine the local magnetization around a single capillary. Here we give a rigorous deviation of the exact time evolution of the signal. The relation to previously developed approximative descriptions of the dephasing process is discussed.

A. Exact solution

Recently, we presented an analytical solution of the Bloch-Torrey Eq. (3) for dephasing in a two-dimensional dipole field [13]. The local transverse magnetization can be given in terms of the eigenfunction expansion

$$\frac{m(r,\phi,t)}{m_0} = e^{-\frac{t}{T_2}}\sum_{m=0}^{\infty}\sum_{n=1}^{\infty} c_{nm} ce_{2m}\left(\phi, i\frac{\delta\omega R_C^2}{2D}\right) \times R_{nm}(r) e^{-\lambda_{nm}^2 \frac{D}{R_C^2} t}, \tag{6}$$

with the initial transverse magnetization m_0. The expansion coefficients are given by

$$\frac{c_{nm}}{2\pi} = \frac{A_0^{(2m)}\lambda_{nm}^2 J'_{k_m}\left(\frac{\lambda_{nm}}{\sqrt{\eta}}\right)\left[J'_{k_m}(\lambda_{nm})s'_{1,k_m}\left(\frac{\lambda_{nm}}{\sqrt{\eta}}\right) - J'_{k_m}\left(\frac{\lambda_{nm}}{\sqrt{\eta}}\right)s'_{1,k_m}(\lambda_{nm})\right]}{\left[J'_{k_m}(\lambda_{nm})\right]^2\left[\lambda_{nm}^2 - \eta k_m^2\right] - \left[J'_{k_m}\left(\frac{\lambda_{nm}}{\sqrt{\eta}}\right)\right]^2\left[\lambda_{nm}^2 - k_m^2\right]}, \tag{7}$$

where s'_{1,k_m} denotes the first derivative of the Lommel function [14] with the indices 1 and k_m. The second index k_m of the Lommel function is also the index of the first derivative of the Bessel functions J'_{k_m}. This index is called the angular eigenvalue

$$k_m^2 = a_{2m}\left(i\delta\omega\frac{R_C^2}{2D}\right), \tag{8}$$

that are given by the characteristic values a_{2m} of the respective Mathieu functions. The characteristic values a_{2m} depend on a purely imaginary parameter that complicates the analysis [15]. A detailed discussion of Mathieu functions and their characteristic values for purely imaginary parameters is given in [16]. In Appendix A simple series expansions for the angular eigenvalues k_m in dependence on the parameter $\delta\omega R_C^2/D$ are given. As an example, for the typical parameters of the human myocardium at 1.5 T ($\delta\omega = 151\,\mathrm{s}^{-1}$, $R_C = 2.75\,\mu$m, and $D = 1\,\mu\mathrm{m}^2\mathrm{ms}^{-1}$) [12,13,17], the ranging parameters take the value $\delta\omega R_C^2/D = 1.141\,94$ and, according to Eq. (8) we obtain for the first angular eigenvalues $k_0 \approx 0.411$, $k_1 \approx 1.964$, and $k_2 \approx 3.998$ (these values can also be obtained from the series expansions given in Appendix A). The higher eigenvalues are approximately $k_m \approx 2m$. In the enumerator of Eq. (7), the symbol $A_0^{(2m)}$ represents the first Fourier coefficient of the even π-periodic Mathieu functions ce_{2m}. The Fourier-expansion of the Mathieu functions is discussed in detail in Ref. [16]. The Fourier-coefficient $A_0^{(2m)}$ depends also on the parameter $\delta\omega R_C^2/D$ and approximations and limiting cases are discussed in detail in Appendix B.

The radial eigenfunctions $R_{nm}(r)$ that appear in Eq. (6) are the solution of the Bessel type eigenvalue equation

$$R_C^2\left[\frac{k_m^2}{r^2} - \Delta_r\right]R_{nm}(r) = \lambda_{nm}^2 R_{nm}(r), \tag{9}$$

with the radial Laplacian $\Delta_r = r^{-1}\partial_r(r\partial_r)$. Thus, the radial eigenfunctions

$$R_{nm}(r) = Y'_{k_m}(\lambda_{nm})\,J_{k_m}\left(\frac{\lambda_{nm}}{R_C}r\right) - J'_{k_m}(\lambda_{nm})\,Y_{k_m}\left(\frac{\lambda_{nm}}{R_C}r\right) \tag{10}$$

are a linear combination of the Bessel function J and Neumann Function Y with the index k_m given in Eq. (8). These radial eigenfunctions given in Eq. (10) fulfill the reflecting boundary conditions at $r = R_C$ [see the left-hand side of Eq. (4)]. To obey the reflecting boundary conditions at the surface of the dephasing cylinder at $r = R_D$ [see the right hand side of Eq. (4)], the radial eigenvalues λ_{nm} have to fulfill the following equation

$$Y'_{k_m}(\lambda_{nm})\,J'_{k_m}\left(\frac{\lambda_{nm}}{\sqrt{\eta}}\right) = J'_{k_m}(\lambda_{nm})\,Y'_{k_m}\left(\frac{\lambda_{nm}}{\sqrt{\eta}}\right), \tag{11}$$

where the index of the Bessel functions is the angular eigenvalue k_m given in Eq. (8). For each angular eigenvalue k_m there exists an infinite number of radial eigenvalus $\lambda_{1m}, \lambda_{2m}, \ldots$ that are purely real values if the angular eigenvalue k_m is real or that are complex if the angular eigenvalue k_m is a complex value. In general, the transcendental Eq. (11) has to be solved numerically which requires sufficiently accurate initial values for the complex root finding. To obtain these initial values, it is convenient to solve the eigenvalue Eq. (9) approximately by discretizing the radial Laplace operator with the reflecting boundary conditions of Eq. (4) in the following form:

$$\hat{\Delta}_r = \frac{1}{h^2}\begin{pmatrix} -\frac{2r_{1\frac{1}{2}}}{r_1} & +\frac{2r_{1\frac{1}{2}}}{r_1} & & & & & & \\ +\frac{r_{1\frac{1}{2}}}{r_2} & -\frac{2r_2}{r_2} & +\frac{r_{2\frac{1}{2}}}{r_2} & & & & & \\ & +\frac{r_{2\frac{1}{2}}}{r_3} & -\frac{2r_3}{r_3} & +\frac{r_{3\frac{1}{2}}}{r_3} & & & & \\ & & \ddots & \ddots & \ddots & & & \\ & & & +\frac{r_{p-2\frac{1}{2}}}{r_{p-2}} & -\frac{2r_{p-2}}{r_{p-2}} & +\frac{r_{p-1\frac{1}{2}}}{r_{p-2}} & & \\ & & & & +\frac{r_{p-1\frac{1}{2}}}{r_{p-1}} & -\frac{2r_{p-1}}{r_{p-1}} & +\frac{r_{p-\frac{1}{2}}}{r_{p-1}} \\ & & & & & +\frac{2r_{p-\frac{1}{2}}}{r_p} & -\frac{2r_{p-\frac{1}{2}}}{r_p} \end{pmatrix}, \tag{12}$$

with the discretization scheme

$$r_j = R_C + [j-1]h \quad \text{for} \quad j = 1,\ldots,p \quad \text{and}$$
$$h = \frac{R_D - R_C}{p-1}.$$

However, for the lowest eigenvalues a simple approximation can be found:

$$\lambda_{1m}^2 \approx \frac{4\eta k_m\left[1-k_m^2\right][\eta^{k_m}-1]}{\left[k_m^2+k_m-2\right][1-\eta][1+\eta^{k_m}] - 2k_m[\eta^{k_m}-\eta]}. \tag{13}$$

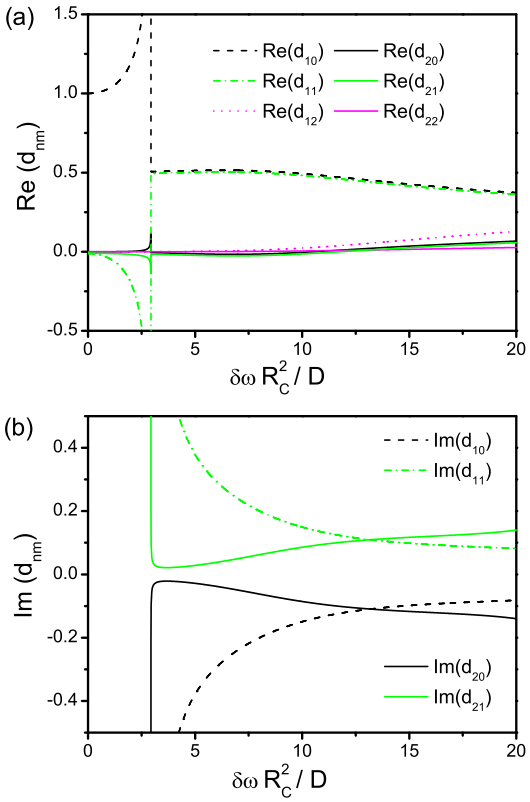

FIG. 2. (Color online) Real part (a) and imaginary part (b) of the expansion coefficients d_{nm} obtained from Eq. (15). Beyond the branching point the corresponding two adjacent expansion coefficients form complex conjugated pairs, e.g., $d_{10} = d_{11}^*$ for $\delta\omega R_C^2/D \geqslant 2.94$.

Evaluating the total signal according to Eq. (5) with the exact solution in Eq. (6) yields

$$\frac{S(t)}{S(0)} = \sum_{m=0}^{\infty}\sum_{n=1}^{\infty} d_{nm} e^{-t[\lambda_{nm}^2 \frac{D}{R_C^2} + \frac{1}{T_2}]}, \tag{14}$$

with the expansion coefficients

$$d_{nm} = \frac{8\eta}{1-\eta} \times \frac{\left[A_0^{(2m)}\right]^2 \left[J'_{k_m}(\lambda_{nm}) s'_{1,k_m}\left(\frac{\lambda_{nm}}{\sqrt{\eta}}\right) - J'_{k_m}\left(\frac{\lambda_{nm}}{\sqrt{\eta}}\right) s'_{1,k_m}(\lambda_{nm})\right]^2}{\left[J'_{k_m}(\lambda_{nm})\right]^2 \left[\lambda_{nm}^2 - \eta k_m^2\right] - \left[J'_{k_m}\left(\frac{\lambda_{nm}}{\sqrt{\eta}}\right)\right]^2 \left[\lambda_{nm}^2 - k_m^2\right]}. \tag{15}$$

In Fig. 2 these expansion coefficients d_{nm} are visualized in dependence on the parameter $\delta\omega R_C^2/D$. For $\delta\omega R_C^2/D \leqslant 2.94$ the expansion coefficients d_{nm} are purely real. In the motional narrowing limit only the first expansion coefficient d_{10} remains:

$$\lim_{\delta\omega R_C^2/D \to 0} d_{nm} = \delta_{n1}\delta_{m0}. \tag{16}$$

Behind the first branching point, two adjacent expansion coefficients form a complex conjugated pair, i.e., $d_{10} = d_{11}^*$ (see black dashed lines and green dash-dotted lines in Fig. 2).

Symmetry properties of the expansion coefficients d_{nm} are given in Eq. (C1) in Appendix C.

For the typical microscopic tissue parameters of the myocardium ($\delta\omega = 151\ \mathrm{s}^{-1}$, $R_C = 2.75\,\mu\mathrm{m}$, and $D = 1\,\mu\mathrm{m}^2\mathrm{ms}^{-1}$) the ranging parameters take the value $\delta\omega R_C^2/D = 1.141\,94$ and all expansion coefficients are purely real. The signal decay according to Eq. (14) is visualized in the blue lines in Figs. 5 and 6.

The initial value of the signal $S(t)$ at $t = 0$ leads to the relation

$$\sum_{m=0}^{\infty}\sum_{n=1}^{\infty} d_{nm} = 1, \tag{17}$$

which can be used to estimate the number of coefficients for a required numerical accuracy. From Eq. (14) it is obvious that the time course of the signal is multiexponential.

B. Strong collision approximation

The strong collision approximation is based on replacing the diffusion operator of the original Bloch-Torrey equation by a simpler stochastic process that allows an easy analysis of the total measurable signal [1,12]. In comparison to other approximations of the dephasing process, the strong collision approximation provides very accurate results over the whole dynamic range [18,19]. The strong collision approximation can in principle be extended to exactly model the diffusion process [5]. Nevertheless, in this approximation it is not possible to analyze the local magnetization $m(r,\phi,t)$. In Ref. [8] the free induction decay of muscle tissue was analyzed, demonstrating significant deviations from the monoexponential behavior for higher field strengths. In dependence of the underlying tissue parameters (capillary radius R_C, frequency shift $\delta\omega$, diffusion coefficient D, and volume fraction η), different dephasing regimes can be distinguished. Here, the relevant parameter for the classification of the dephasing regimes is the product $\tau\delta\omega$ with the correlation time [20]

$$\tau = \frac{R_C^2}{4D}\frac{\ln(\eta)}{\eta - 1}. \tag{18}$$

For the considered parameters of the myocardium ($\delta\omega = 151\ \mathrm{s}^{-1}$, $R_C = 2.75\,\mu\mathrm{m}$, and $D = 1\,\mu\mathrm{m}^2\mathrm{ms}^{-1}$) at a field strength of 1.5 T, the correlation time takes the value $\tau = 5.1$ ms. With the volume fraction $\eta = 0.084$ it can be found that the underlying dephasing regime in the myocardium is the fast diffusion regime (see Eq. (21) in Ref. [8]). The derived analytical expression for the signal $S_{\mathrm{SC}}(t)$ in the strong collision approximation (index SC) is

$$\frac{S_{\mathrm{SC}}(t)}{S_{\mathrm{SC}}(0)} = e^{-t[\frac{1}{\tau} + \frac{1}{T_2}]}\left[\frac{\alpha}{\tau\Omega}\sinh(\Omega t) + h(t)\right], \tag{19}$$

with the parameters

$$\alpha = \frac{2}{[1-\eta]^2}\left[1 + \eta^2 - \eta\frac{2 + \tau^2\delta\omega^2[1-\eta]^2}{\sqrt{1 + \tau^2\delta\omega^2[1-\eta]^2}}\right], \tag{20}$$

$$\Omega = \frac{\sqrt{1 + \eta^2 - 2\eta\sqrt{1 + \tau^2\delta\omega^2[1-\eta]^2}}}{\tau[1-\eta]}, \tag{21}$$

and the function

$$h(t) = \frac{2}{\pi}\int_{\eta}^{1} dx\ \frac{\sin(x\,\delta\omega\,t)\sqrt{x^2-\eta^2}}{x^2[1-\eta]+\frac{1+\eta}{[\tau\delta\omega]^2}-\frac{2\eta}{\tau\,\delta\omega}\sqrt{1-x^2}} + \frac{2}{\pi}\int_{1}^{\infty} dx \frac{\sin(x\,\delta\omega\,t)[\sqrt{x^2-\eta^2}+\eta\sqrt{x^2-1}]}{\frac{x^2[1+\eta^2]+2\eta[\sqrt{[x^2-\eta^2][x^2-1]}-\eta]}{1+\eta}+\frac{1+\eta}{[\tau\delta\omega]^2}}. \tag{22}$$

In contrast to the exact solution, the signal is not purely multiexponentially decaying but exhibits analogies to the damped driven harmonic oscillator.

C. Gaussian approximation

In the Gaussian approximation (index GA), the signal can be written in terms of the correlation function

$$\frac{S_{\mathrm{GA}}(t)}{S_{\mathrm{GA}}(0)} = \mathrm{e}^{-\frac{t}{T_2}}\exp\left(-\int_0^t d\xi[t-\xi]K(\xi)\right). \tag{23}$$

For diffusion between two concentric cylinders in Krogh's capillary model, the correlation function can be expressed as [21]

$$K(\xi) = \delta\omega^2\sum_{n=1}^{\infty} G_n \mathrm{e}^{-\kappa_n^2\frac{D\xi}{R_C^2}}, \tag{24}$$

where the eigenvalues κ_n are a solution of the equation

$$J_2'(\kappa_n)Y_2'\left(\frac{\kappa_n}{\sqrt{\eta}}\right) = J_2'\left(\frac{\kappa_n}{\sqrt{\eta}}\right)Y_2'(\kappa_n). \tag{25}$$

This eigenvalue equation has the same structure as Eq. (11) and, thus, in analogy to Eq. (9) the values κ_n^2 are the eigenvalues of the Bessel-operator $R_C^2[4/r^2-\Delta_r]$ with Neumann boundary conditions. For numerical determination of these eigenvalues, the same discretization scheme as described above can be used. The eigenvalues κ_n depend on the volume fraction η only and are visualized in Fig. 3(a).

The expansion coefficients of the correlation function Eq. (24) are given by

$$G_n = \frac{8}{1-\eta}\frac{1}{\kappa_n^2}\frac{\left[\sqrt{\eta}J_2'\left(\frac{\kappa_n}{\sqrt{\eta}}\right)-\eta^2 J_2'(\kappa_n)\right]^2}{\left[4-\kappa_n^2\right]\left[J_2'\left(\frac{\kappa_n}{\sqrt{\eta}}\right)\right]^2+\left[\kappa_n^2-4\eta\right]\left[J_2'(\kappa_n)\right]^2}. \tag{26}$$

These expansion coefficients depend on the eigenvalue κ_n, and, thus, they only depend on the volume fraction as shown in Fig. 3(b). Introducing the correlation function given in Eq. (24) into the general expression for the signal decay given in Eq. (23) one gets the following expression for the signal decay in the Gaussian approximation:

$$\frac{S_{\mathrm{GA}}(t)}{S_{\mathrm{GA}}(0)} = e^{-\frac{t}{T_2}}\exp\left(-\left[\frac{\delta\omega R_C^2}{D}\right]^2 \times\sum_{n=1}^{\infty}\frac{G_n}{\kappa_n^2}\left[\frac{Dt}{R_C^2}+\frac{e^{-\kappa_n^2\frac{Dt}{R_C^2}}-1}{\kappa_n^2}\right]\right). \tag{27}$$

Similar to the expressions for the exact analytical solution and to the expression for the Gaussian approximation, this expression depends only on the microscopic parameters of the underlying tissue.

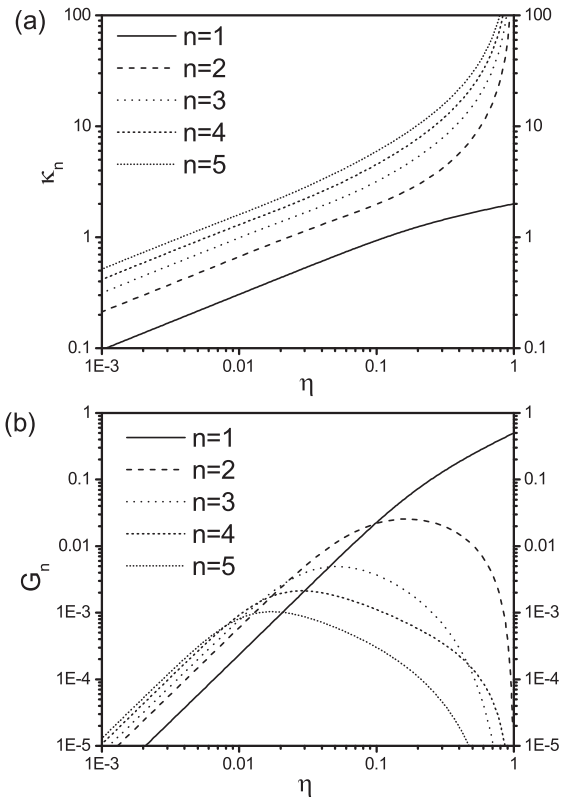

FIG. 3. Eigenvalues κ_n obtained from Eq. (25) and expansion coefficients G_n obtained from Eq. (26) in dependence on the volume fraction η.

IV. MONOEXPONENTIAL DECAY AND T_2^*-RELAXATION

For small values of the parameter $\delta\omega R_C^2/D$, the signal decay is purely multiexponentially or exhibits only small oscillating components. In this case, the signal decay can be approximated by a monoexponential decay with the characteristic relaxation time T_2^* in the following form:

$$\frac{S(t)}{S(0)} = e^{-\frac{t}{T_2^*}}. \tag{28}$$

For small values of the parameter $\delta\omega R_C^2/D$, the underlying diffusion regime is given by the motional narrowing regime with monoexponential relaxation rate:

$$\frac{1}{T_2^*} = \frac{1}{T_2} + \tau\langle\omega^2(r,\phi)\rangle = \frac{1}{T_2} + \frac{\eta}{2}\tau\delta\omega^2, \tag{29}$$

whereas the correlation time τ is given in Eq. (18). In the opposite limit of negligible diffusion, the static dephasing regime, spins are always located on the same position and the relaxation rate is determined by [22]

$$\frac{1}{T_2^*} = \frac{1}{T_2} + \frac{2\eta\delta\omega}{1+\eta}. \tag{30}$$

From the monoexponential decay the relaxation time can be obtained in terms of the mean relaxation time

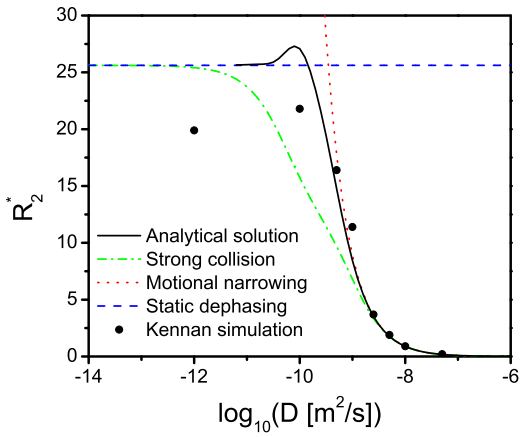

FIG. 4. (Color online) Dependence of the transverse relaxation rate R_2^* on diffusion coefficient D in comparison with data from Kennan *et al.* [24] for simulation parameters: volume fraction $\eta = 0.05$, capillary radius $R_C = 2.5\,\mu$m, frequency shift $\delta\omega = 269\,\mathrm{s}^{-1}$, and intrinsic relaxation time $T_2 = \infty$. The black line is the exact analytical solution obtained from Eq. (32) and the green (dash-dotted) line represents the strong collision approximation obtained from Eq. (35). Limiting cases are the motional narrowing regime [red (dotted) line from Eq. (29)] and the static dephasing regime [blue (dashed) line from Eq. (30)].

approximation [6]:

$$T_2^* = \int_0^\infty dt\, \frac{S(t)}{S(0)}. \tag{31}$$

With this definition at hand, the monoexponential relaxation time can be given for the exact analytical signal, the strong-collision approximation, and for the Gaussian approximation, respectively.

The exact analytical signal time decay is given as

$$T_2^* = \sum_{m=0}^{\infty}\sum_{n=1}^{\infty} \frac{d_{nm}}{\frac{\lambda_{nm}^2 D}{R_C^2} + \frac{1}{T_2}}, \tag{32}$$

which directly follows from introducing Eq. (14) into Eq. (31). Furthermore, the exact form of the transverse relaxation time is in agreement with general scaling laws [23]. The analytical results are compared with simulation data of transverse relaxation by Kennan *et al.* [24] in Fig. 4 as well as the strong collision approximation and the limiting cases (static dephasing and motional narrowing regime) for the same parameters. As seen in Fig. 4, the new analytical results describe the relaxation process nicely in comparison with the simulation data, and the limiting cases are perfectly reproduced.

Since the leading addend in the sum Eq. (14) is the exponential decay with the coefficient d_{10} (see Fig. 2), the free induction decay can be approximated by $S(t) \approx S(0)\exp(-t[\lambda_{10}^2 D/R_C^2 + 1/T_2])$. Thus, with the approximation for the first eigenvalue given in Eq. (13) one obtains for the transverse relaxation time the expression

$$\frac{1}{T_2^*} \approx \frac{1}{T_2} + \frac{D}{R_C^2}\frac{4\eta k_0\left[1-k_0^2\right][\eta^{k_0}-1]}{\left[k_0^2+k_0-2\right][1-\eta][1+\eta^{k_0}] - 2k_0[\eta^{k_0}-\eta]}, \tag{33}$$

where the first angular eigenvalue k_0 can be approximated by

$$k_0 \approx \frac{\delta\omega R_C^2/D}{2\sqrt{2}} + \frac{7\left[\delta\omega R_C^2/D\right]^3}{1024\sqrt{2}} + \frac{3271\left[\delta\omega R_C^2/D\right]^5}{943\,718\,4\sqrt{2}}, \tag{34}$$

for $\delta\omega R_C^2/D < 2.94$.

In the strong collision approximation, the monoexponential relaxation time is given by [12]

$$\frac{1}{T_2^*} = \frac{1}{T_2} + \frac{1}{\tau}\frac{\sqrt{1+\eta^2\tau^2\delta\omega^2} + \eta\sqrt{1+\tau^2\delta\omega^2} - 1 - \eta}{1+\eta}, \tag{35}$$

where the correlation time τ is given in Eq. (18).

To obtain the T_2^*-relaxation time in the Gaussian approximation, the signal decay from Eq. (27) has to be inserted into the definition Eq. (31) of the mean relaxation time approximation yielding

$$T_2^* = \int_0^\infty dt \exp\left(-\frac{t}{T_2} - \left[\frac{\delta\omega R_C^2}{D}\right]^2 \times \sum_{n=1}^{\infty}\frac{G_n}{\kappa_n^2}\left[\frac{Dt}{R_C^2} + \frac{e^{-\kappa_n^2\frac{Dt}{R_C^2}} - 1}{\kappa_n^2}\right]\right), \tag{36}$$

which cannot be simplified.

V. EXPERIMENTAL VERIFICATION

To validate the analytical results, we performed measurements of the free induction decay in rat skeletal muscle as well as the myocardium of mice. We chose these kinds of muscle tissue, since the capillaries are then highly ordered and the assumptions of Krogh's capillary model are valid. For cardiac muscle tissue, the septal region of the heart was chosen where the capillaries are arranged approximately in perpendicular to the external magnetic field [25] and signal distortions due to background gradients are minimized.

A. Animal handling

All measurements with animals were performed in accordance with European regulations on the care and use of laboratory animals. The animal measurements were performed with a 7 T Bruker Biospec small animal MRI system (Bruker Biospin, Ettlingen, Germany). The scanner was equipped with an imaging gradient system with a maximum gradient of 397 mT/m. A 40-mm quadrature birdcage resonator for mouse imaging as well as a 72-mm quadrature birdcage resonator for rat imaging were used for radio frequency transmission and signal reception.

B. Skeletal muscle

For the measurements of rat skeletal muscle tissue, anesthesia was induced with 4% isoflurane in oxygen in a healthy Wistar rat and maintained with 2% isoflurane in oxygen. The hind limb of the animal was placed as perpendicular as possible to the main magnetic field in the center of the birdcage resonator. This ensured a perpendicular orientation of the capillaries in the muscle with respect to the main magnetic

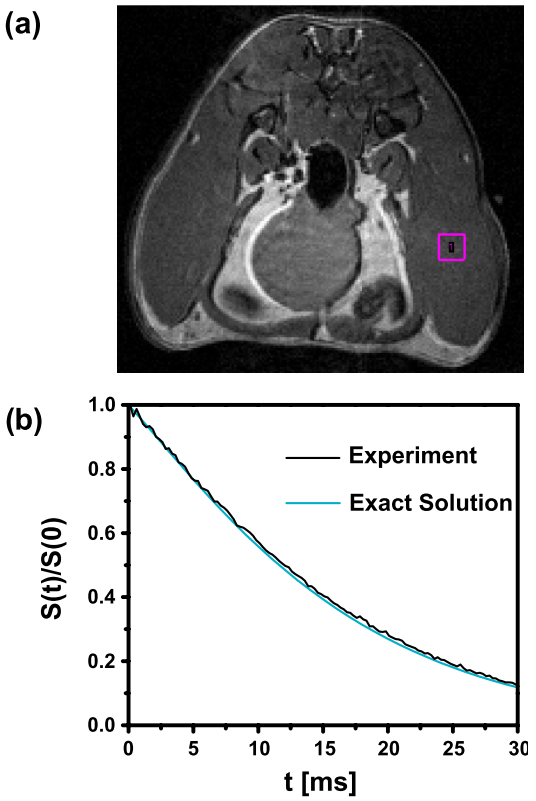

FIG. 5. (Color online) Anatomical image of the hind limbs of a rat in axial view (a) with the selected PRESS voxel. The black solid line in panel (b) is the measured time evolution of the free induction decay, obtained from the selected voxel in the hind limb. The blue (gray) solid line is the exact signal decay obtained from Eq. (14) with the typical parameters given in Table II and the measured intrinsic relaxation time $T_2 = 22.3$ ms.

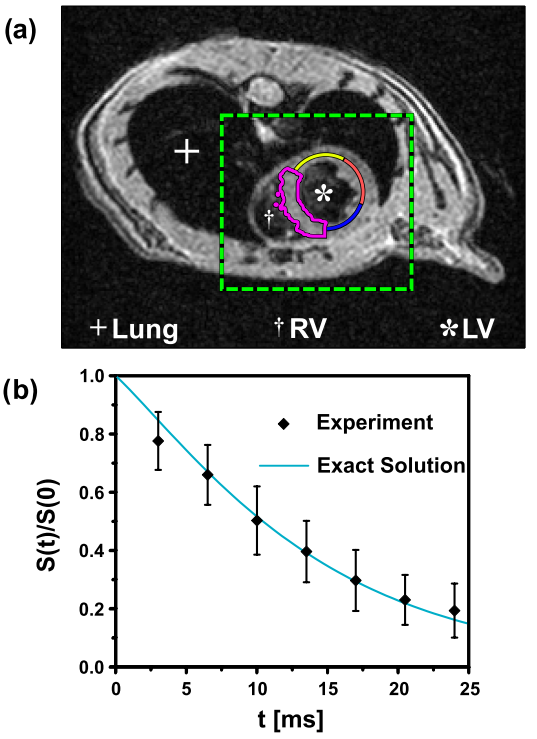

FIG. 6. (Color online) Anatomical image of the heart in short axis view (a) with the left ventricle (LV,∗), the right ventricle (RV,†), and the septum [encircled with a magenta (medium gray) line], surrounded by lung tissue (+). (b) The measured values (black diamonds) are compared with the exact signal decay [blue (gray) solid line] obtained from Eq. (14) with the typical parameters given in Table II. Also, the walls of the left ventricle are highlighted in colors as anterior wall [blue (dark gray)], lateral wall [red (medium gray)] and posterior wall [yellow (light gray)]. The dashed-green image segment is used in Fig. 7 for the visualization of voxelwise relaxation time maps.

field. Vital functions were monitored with a pressure balloon. For the measurement in the skeletal muscle, no synchronization with respiratory or cardiac motion was necessary. In the central part of the left thigh muscle a cubic voxel of the size 2.5 mm × 2.5 mm × 2.5 mm was selected. A PRESS sequence with repetition time $T_R = 6$ s, echo time $T_E = 9.9$ ms, and eight averages was used to obtain the FID from this voxel [see magenta box in Fig. 5(a)]. The T_2 relaxation time was measured with the PRESS sequence with similar parameters to the FID measurement but different echo times $T_E = (12,15,20,25)$ ms and only one average.

C. Myocardial tissue

For cardiac relaxation time mapping, anesthesia was initiated in a healthy BL/6 mouse using 4% isoflurane in oxygen and maintained with 2% isoflurane in oxygen. Vital functions were monitored using an electrocardiogram and a pressure balloon. Imaging was synchronized to the heart cycle by prospectively triggering the excitation pulse to the end diastolic phase of the heart cycle. Respiratory motion corruption was avoided by gating out the acquisition to the breath hold. After localizing a midventricular short axis slice [see Fig. 6(a)] a multigradient echo sequence was used for cardiac T_2^* mapping and a Carr-Purcell-Meiboom-Gill sequence for T_2 mapping. The corresponding parameters are given in Table I.

D. Data analysis

All data was analyzed using Matlab (The MathWorks Inc., Natick, MA, USA). Relaxation time parameters were determined by a nonlinear least-square fit of the signal model $S(t) = Ae^{-t/T}$ to the aquired data where T is either T_2 or T_2^*.

TABLE I. Measurement parameters for the T_2 and T_2^* mapping in the mouse (†excitation/refocusing pulse; ‡first echo/remaining echos).

Parameter	T_2^*	T_2
Repetition time T_R [ms]	100	1250
Flip angle [°]	30	90/180†
In-plane resolution [μm × μm]	200 × 200	200 × 200
Slice thickness [mm]	0.25	1.00
Field of view [mm]	25.6 × 19.2	25.6 × 19.2
Inter echo time [ms]	3.0/3.5‡	5.5
Echo number	12	8

TABLE II. Microscopic parameters of myocardial tissue and skeletal muscle tissue at an external magnetic field strength $B_0 = 7\,\mathrm{T}$.

Microscopic parameter	Myocardium	Skeletal muscle
Volume fraction	$\eta = 0.15$	$\eta = 0.08$
Capillary radius	$R_C = 2.75\,\mu\mathrm{m}$	$R_C = 4.00\,\mu\mathrm{m}$
Diffusion coefficient	$D = 1\,\mu\mathrm{m}^2\mathrm{ms}^{-1}$	$D = 1\,\mu\mathrm{m}^2\mathrm{ms}^{-1}$
Frequency shift	$\delta\omega = 330\,\mathrm{s}^{-1}$	$\delta\omega = 330\,\mathrm{s}^{-1}$
Intrinsic relaxation time	$T_2 = 22.0\,\mathrm{ms}$	$T_2 = 22.3\,\mathrm{ms}$
Correlation time, Eq. (18)	$\tau = 4.2\,\mathrm{ms}$	$\tau = 11.0\,\mathrm{ms}$
Method for T_2^*	Myocardium	Skeletal muscle
Exact solution, Eq. (32)	$T_2^* = 13.9\,\mathrm{ms}$	$T_2^* = 14.7\,\mathrm{ms}$
Lowest eigenvalue, Eq. (33)	$T_2^* = 12.1\,\mathrm{ms}$	$T_2^* = 9.4\,\mathrm{ms}$
Strong collision, Eq. (35)	$T_2^* = 13.9\,\mathrm{ms}$	$T_2^* = 14.9\,\mathrm{ms}$
Gaussian, Eq. (36)	$T_2^* = 14.3\,\mathrm{ms}$	$T_2^* = 14.9\,\mathrm{ms}$
Motional Narrowing, Eq. (29)	$T_2^* = 12.6\,\mathrm{ms}$	$T_2^* = 10.8\,\mathrm{ms}$
Static Dephasing, Eq. (30)	$T_2^* = 7.6\,\mathrm{ms}$	$T_2^* = 10.7\,\mathrm{ms}$
Experimental value	$T_2^* = 13.2\,\mathrm{ms}$	$T_2^* = 15.8\,\mathrm{ms}$

To prevent bias in the T_2^* mapping, only the first 7 echos are used since the remaining echos are dominated by noise.

E. Experimental results

In Table II, the monoexponential relaxation times as well as all relevant microscopic parameters to determine signal formation are presented. The free induction decay measured with the PRESS sequence in rat hind limb is shown in Fig. 5 and is compared with the analytical model: experimental and model values show an excellent agreement. For computation of the free induction decay according to Eq. (14), we used the experimentally measured intrinsic T_2 relaxation time $T_2 = 22.3\,\mathrm{ms}$; see Table II.

Furthermore, for mouse myocardium, it can be seen from Fig. 6 that the exact analytical result coincides well with the measured values of the free induction decay. The quantification of the transverse relaxation by a monoexponential relaxation time enables us to visualize the physiological properties of the myocardium in terms of a T_2^* map as shown in Fig. 7. The susceptibility effects of the surrounding lung tissue shorten the T_2^*-relaxation time in the anterior and posterior wall, while the septal region exhibits nearly homogeneous relaxation times [26]. Furthermore, in the septal region the capillaries are nearly perpendicular to the external field, which maximizes the susceptibility effect due to the magnetic properties of the blood inside the capillaries that are responsible for the measured dephasing effects.

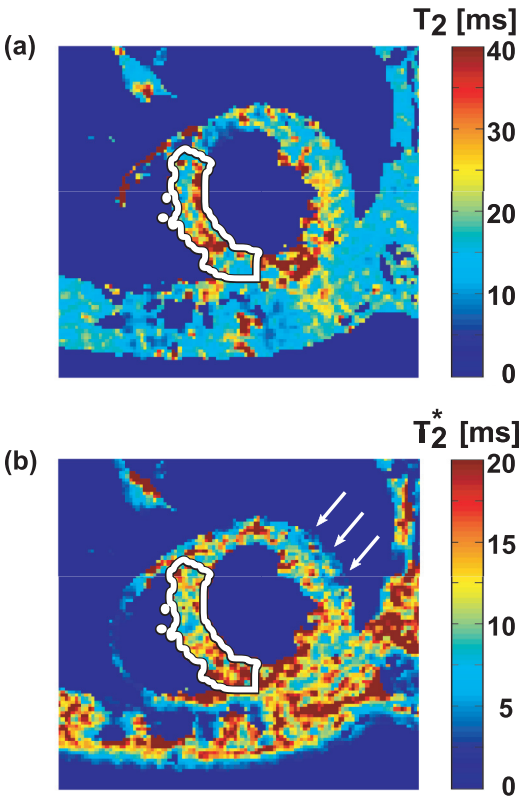

FIG. 7. (Color) Quantitative T_2 map (a) and T_2^* map (b) of the myocardium corresponding to the green-dashed image segment of the anatomical image Fig. 6(a). A significant reduction of the T_2^* relaxation time due to background gradients at the boundary between heart and surrounding lung tissue is clearly visible (see white arrows). This effect is not observed in the septal region.

VI. DISCUSSION

The presented analytical model of spin dephasing in muscle tissue allows the correct description of the free induction decay and accurate quantification of transverse relaxation time depending on the microstructural parameters of the tissue. In contrast to previous models all diffusion regimes are included without any simplifying assumptions on the diffusive movement of the involved spins. The limiting cases (motional narrowing and static dephasing) are adequately reproduced as can be seen in Fig. 4. Furthermore, in the intermediate diffusion regime the presented exact analysis of the dephasing process reproduces the simulation data from Ref. [24] more accurately than the previously developed strong collision approximation.

The measured free induction decay in skeletal muscle as well as myocardial tissue agrees very well with analytical predictions for the exact free induction decay [given in Eq. (14)]. This can also be seen from the transverse relaxation times determined with the different methods as shown in Table II. Additionally the relaxation time obtained from the analytical exact solution compares well with the relaxation times from strong collision approximation and Gaussian approximation (Table II). The deviation between the exact signal evolution and the approximative solution is explained by the microscopic parameters of the myocardium and the strength of the external magnetic field, which govern the dephasing regime. For small values of the parameter $\delta\omega R_C^2/D$, e.g., low field strengths as used in clinical routine and small susceptibility differences, all eigenvalues are purely real resulting in monotonic decay of the free induction decay. This is supported by the fact that for the clinical magnetic field strength of 1.5 T, this parameter takes the value $\delta\omega R_C^2/D \approx 1.14194$ and, thus, the underlying diffusion regime is the fast diffusion regime where diffusion effects dominate over susceptibility effects. In this diffusion regime, the strong collision approximation and the Gaussian approximation are valid, as recently confirmed by numerical

solution of the dephasing process [27]. Since the strong collision approximation as well as the Gaussian approximation are valid for the diffusion dominating dephasing regime [28], it is obvious that the exact analytic solution and the strong collision approximation and the Gaussian approximation coincide. Nevertheless, for an increasing influence of susceptibility effects that can be obtained by higher field strengths or lower oxygenation levels, the deviations to the exact analytic solution become more substantial.

VII. SUMMARY AND CONCLUSIONS

In summary, we presented an exact analytical solution of the free induction decay in muscle tissue that was experimentally verified in mouse myocardium and rat skeletal muscle. Simple expressions are given for the transverse relaxation time T_2^* in dependence on the physiological parameters. Measured values of the free induction decay in both mouse myocardial and rat skeletal muscle are in good agreement with the analytically exact values. The theoretical results can easily be adapted to determine the microstructure of spatially or magnetically heterogeneous media, where the basic primitive cell consists of a single cylindrical object that generates a two-dimensional dipole field.

Furthermore, it could be clarified, under which circumstances the oscillating components of the signal decay can be observed: this issue is closely connected to the angular eigenvalue spectrum and the properties of the characteristic values of the Mathieu functions for purely imaginary parameters, which exhibits a complicated branching structure. Since these eigenvalues can become complex, the signal consequently decays with a complex eigenvalue that corresponds to the oscillating components.

APPENDIX A: APPROXIMATIONS OF THE ANGULAR EIGENVALUES

The angular eigenvalues k_m can be obtained from the characteristic values of the Mathieu functions as shown in Eq. (8). These eigenvalues are the index of the Bessel functions that appear in the radial eigenfunctions $R_{nm}(r)$ in Eq. (10), and, hence in the radial eigenvalue Eq. (11). For small values of the parameter $\delta\omega R_C^2/D$ the first angular eigenvalues can be approximated by

$$m=0:\ k_0 \approx \frac{\delta\omega R_C^2/D}{2\sqrt{2}} + \frac{7\left[\delta\omega R_C^2/D\right]^3}{1\,024\sqrt{2}} + \frac{3\,271\left[\delta\omega R_C^2/D\right]^5}{9\,437\,184\sqrt{2}},$$

$$m=1:\ k_1 \approx 2 - \frac{5\left[\delta\omega R_C^2/D\right]^2}{192} - \frac{913\left[\delta\omega R_C^2/D\right]^4}{884\,736},$$

$$m=2:\ k_2 \approx 4 - \frac{\left[\delta\omega R_C^2/D\right]^2}{960} + \frac{209\left[\delta\omega R_C^2/D\right]^4}{55\,296\,000},$$

$$m=3:\ k_3 \approx 6 - \frac{\left[\delta\omega R_C^2/D\right]^2}{3\,360} + \frac{1\,123\left[\delta\omega R_C^2/D\right]^4}{75\,866\,112\,000}.$$

These approximations are valid for values of the parameter $\delta\omega R_C^2/D$ before the according branching point. The series expansion for the higher angular eigenvalues can be obtained from Eq. (27) in Ref. [16]:

$$k_m \approx 2m - \frac{[\delta\omega R_C^2/D]^2}{32m[4m^2-1]} \quad \text{for} \quad \delta\omega R_C^2/D < p_{\lfloor \frac{m}{2} \rfloor}. \tag{A1}$$

The higher angular eigenvalues are $k_m \approx 2m$. In the motional narrowing limit the angular eigenvalues are the even natural numbers: $\lim_{\delta\omega R_C^2/D\to 0} k_m = 2m$.

For large values of the parameters $\delta\omega R_C^2/D$ behind the according branching point, the eigenvalues form a complex conjugated pair

$$k_1 = k_0^* \quad \text{for} \quad \frac{\delta\omega R_C^2}{D} > p_0 \approx 2.94, \tag{A2}$$

$$k_{2l+1} = k_{2l}^* \quad \text{for} \quad \frac{\delta\omega R_C^2}{D} > p_l, \quad \text{with} \tag{A3}$$

$$k_{2l}^2 \approx [4l+1][1+i]\sqrt{\frac{\delta\omega R_C^2}{D}} - i\frac{\delta\omega R_C^2}{D} - 2l^2 - l - \frac{1}{4} \tag{A4}$$

(see Eqs. (32) and (33) in Ref. [16]), where the values for the branching points p_l can be obtained from Table I in Ref. [16] or from Table I in Ref. [13].

APPENDIX B: APPROXIMATIONS OF THE FOURIER COEFFICIENTS

For arbitrary values of the parameter $\delta\omega R_C^2/D$ the first Fourier coefficients $A_0^{(2m)}$ are visualized in Fig. 8. For small values of the parameter $\delta\omega R_C^2/D$ the Fourier coefficients are either purely real or purely imaginary and the can be approximated by

$$m=0:\ A_0^{(0)} \approx \frac{1+\left[\delta\omega R_C^2/[8D]\right]^2}{\sqrt{2}},$$

$$m=1:\ A_0^{(2)} \approx \frac{i\,\delta\omega R_C^2}{8D},$$

$$m=2:\ A_0^{(4)} \approx -\frac{\left[\delta\omega R_C^2/D\right]^2}{768},$$

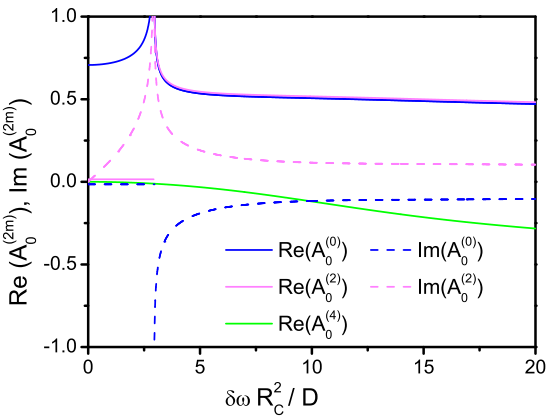

FIG. 8. (Color online) Real part and imaginary part of the Fourier coefficients $A_0^{(2m)}$.

where these expansions are valid before the according branching point. The series expansion of the Fourier coefficients for $m \geqslant 1$ is in general given by

$$A_0^{(2m)} \approx i^m \frac{\left[\delta\omega R_C^2/[8D]\right]^m}{[2m-1]!m} \quad \text{for} \quad \delta\omega R_C^2/D < p_{\lfloor \frac{m}{2} \rfloor}. \tag{B1}$$

In the motional narrowing limit only the first Fourier coefficient $A_0^{(0)}$ remains:

$$\lim_{\delta\omega R_C^2/D \to 0} A_0^{(2m)} = \frac{\delta_{m0}}{\sqrt{2}}, \tag{B2}$$

which can also be seen from Fig. 8. The Fourier coefficients for arbitrary indices take the limit $\lim_{\delta\omega R_C^2/D\to 0} A_{2r}^{(2m)} = \delta_{mr}$ for $r \geqslant 1$. This is visualized in Fig. 6 in Ref. [16] for $r = 1$.

Behind the first branching point ($\delta\omega R_C^2/D > p_0 \approx 2.94$), the Fourier coefficients $A_0^{(2)}$ and $A_0^{(0)}$ are complex conjugated (see also Fig. 8),

$$A_0^{(2)} = A_0^{(0)*} \quad \text{for} \quad \delta\omega R_C^2/D > p_0 \approx 2.94\,, \tag{B3}$$

and can be approximated by

$$A_0^{(0)} \approx \left[2\pi^2 \frac{\delta\omega R_C^2}{D}\right]^{-\frac{1}{8}} e^{-i\frac{\pi}{16}} \quad \text{for} \quad \frac{\delta\omega R_C^2}{D} > p_0 \approx 2.94. \tag{B4}$$

An analogous relation is valid for the higher Fourier coefficient:

$$A_0^{(4l+2)} = A_0^{(4l)*} \quad \text{for} \quad \delta\omega R_C^2/D > p_l, \tag{B5}$$

which can be approximated by

$$A_0^{(4l)} \approx [-1]^l \frac{\sqrt{[4l]!}}{[2l]!4^l} \left[\frac{\pi^2}{2}\frac{\delta\omega R_C^2}{D}\right]^{-\frac{1}{8}} e^{-i\frac{\pi}{16}} \quad \text{for} \quad \frac{\delta\omega R_C^2}{D} > p_l. \tag{B6}$$

A further useful relation that can be used to check the number of coefficients for a sufficient numerical accuracy is

$$\sum_{m=0}^{\infty} A_0^{(2m)} \mathrm{ce}_{2m}\left(\phi, i\delta\omega\frac{R_C^2}{2D}\right) = \frac{1}{2}, \tag{B7}$$

which directly follows from the more general expression

$$\sum_{m=0}^{\infty} A_{2p}^{(2m)} \mathrm{ce}_{2m}\left(\phi, i\delta\omega\frac{R_C^2}{2D}\right) = \cos(2p\phi) - \frac{\delta_{p0}}{2}. \tag{B8}$$

This expression can easily obtained by introducing the Fourier series of the Mathieu function in the form $\mathrm{ce}_{2m}(\phi, i\delta\omega R_C^2/[2D]) = \sum_{r=0}^{\infty} A_{2r}^{(2m)} \cos(2r\phi)$ and using the orthonormality relationship $\sum_{m=0}^{\infty} A_{2p}^{(2m)} A_{2r}^{(2m)} = \delta_{pr} - \delta_{0p}\delta_{0r}/2$. For a given value of the parameter $\delta\omega R_C^2/D$, the left-hand side of Eq. (B7) can be plotted over the angle ϕ to check if the number of indices m for numerical computation is sufficient for each angle.

APPENDIX C: SYMMETRY OF THE EXPANSION COEFFICIENTS

In general, the expansion coefficients d_{nm} given in Eq. (15) exhibit the following symmetry relation:

$$d_{n\,2l+1} = d_{n\,2l}^* \quad \text{for} \quad \delta\omega R_C^2/D > p_l, \tag{C1}$$

which directly follows from the symmetry properties of the angular eigenvalues [see Eq. (A3)] and Fourier coefficients [see Eq. (B5)]. Using the symmetry relations in Eq. (C1) and the properties of the radial eigenvalues (see Eq. (B4) in Ref. [13]), the total signal can be written in the form

$$\begin{aligned}\frac{S(t)}{S(0)} = {} & 2\sum_{m=0}^{l}\sum_{n=1}^{\infty} \mathrm{Re}(d_{n\,2m}) \cos\left(\mathrm{Im}\left(\lambda_{n\,2m}^2\right)\frac{Dt}{R_C^2}\right) e^{-t[\mathrm{Re}(\lambda_{n\,2m}^2)\frac{D}{R_C^2}+\frac{1}{T_2}]} \\ & + 2\sum_{m=0}^{l}\sum_{n=1}^{\infty} \mathrm{Im}(d_{n\,2m}) \sin\left(\mathrm{Im}\left(\lambda_{n\,2m}^2\right)\frac{Dt}{R_C^2}\right) e^{-t[\mathrm{Re}(\lambda_{n\,2m}^2)\frac{D}{R_C^2}+\frac{1}{T_2}]} \\ & + \sum_{m=2l+2}^{\infty}\sum_{n=1}^{\infty} d_{nm} e^{-t[\lambda_{nm}^2\frac{D}{R_C^2}+\frac{1}{T_2}]} \quad \text{for} \quad p_l < \frac{\delta\omega R_C^2}{D} < p_{l+1}.\end{aligned}$$

Similar to Eq. (17) the total signal at $t = 0$ leads to the Parseval-relation

$$2\sum_{m=0}^{l}\sum_{n=1}^{\infty} \mathrm{Re}(d_{n\,2m}) + \sum_{m=2l+2}^{\infty}\sum_{n=1}^{\infty} d_{nm} = 1 \quad \text{for} \quad p_l < \frac{\delta\omega R_C^2}{D} < p_{l+1},$$

which can be used to estimate the number of coefficients for a required numerical accuracy.

[1] W. R. Bauer, W. Nadler, M. Bock, L. R. Schad, C. Wacker, A. Hartlep, and G. Ertl, Magn. Reson. Med. **41**, 51 (1999).

[2] R. J. S. Brown, Phys. Rev. **121**, 1379 (1963).

[3] D. A. Yablonskiy and E. M. Haacke, Magn. Reson. Med. **32**, 749 (1994).

[4] W. R. Bauer, W. Nadler, M. Bock, L. R. Schad, C. Wacker, A. Hartlep, and G. Ertl, Magn. Reson. Med. **42**, 1004 (1999).

[5] W. R. Bauer and W. Nadler, Phys. Rev. E **65**, 066123 (2002).

[6] W. Nadler and K. Schulten, J. Chem. Phys. **82**, 151 (1985).

[7] C. H. Ziener, T. Kampf, G. Melkus, V. Herold, T. Weber, G. Reents, P. M. Jakob, and W. R. Bauer, Phys. Rev. E **76**, 031915 (2007).
[8] C. H. Ziener, T. Kampf, G. Melkus, P. M. Jakob, H.-P. Schlemmer, and W. R. Bauer, Magn. Reson. Imag. **30**, 540 (2012).
[9] A. Krogh, J. Physiol. (London) **52**, 409 (1919).
[10] J. R. Reichenbach and E. M. Haacke, NMR Biomed. **14**, 453 (2001).
[11] H. C. Torrey, Phys. Rev. **104**, 563 (1956).
[12] W. R. Bauer, W. Nadler, M. Bock, L. R. Schad, C. Wacker, A. Hartlep, and G. Ertl, Phys. Rev. Lett. **83**, 4215 (1999).
[13] C. H. Ziener, T. Kampf, G. Reents, H.-P. Schlemmer, and W. R. Bauer, Phys. Rev. E **85**, 051908 (2012).
[14] C. H. Ziener and H.-P. Schlemmer, Integr. Transf. Spec. F. **24**, 141 (2013).
[15] A. M. Berezman, M. K. Kerimov, S. L. Skorokhodov, and G. A. Shadrin, USSR Comput. Math. Math. Phys. **26**, 48 (1986).
[16] C. H. Ziener, M. Rückl, T. Kampf, W. R. Bauer, and H.-P. Schlemmer, J. Comput. Appl. Math. **236**, 4513 (2012).
[17] R. Wassmuth, M. Prothmann, W. Utz, M. Dieringer, F. von Knobelsdorff-Brenkenhoff, A. Greiser, and J. Schulz-Menger, J. Cardiovasc. Magn. Reson. **15**, 27 (2013).
[18] J. D. Dickson, T. W. J. Ash, G. B. Williams, A. L. Sukstanskii, R. E. Ansorge, and D. A. Yablonskiy, J. Magn. Reson. **212**, 17 (2011).
[19] F. T. Kurz, T. Kampf, S. Heiland, M. Bendszus, H. P. Schlemmer, and C. H. Ziener, Magn. Reson. Med. **71**, 1888 (2014).
[20] C. H. Ziener, W. R. Bauer, G. Melkus, T. Weber, V. Herold, and P. M. Jakob, Magn. Reson. Imag. **24**, 1341 (2006).
[21] C. H. Ziener, T. Kampf, V. Herold, P. M. Jakob, W. R. Bauer, and W. Nadler, J. Chem. Phys. **129**, 014507 (2008).
[22] C. H. Ziener, W. R. Bauer, and P. M. Jakob, Magn. Reson. Mater. Phy. **18**, 225 (2005).
[23] C. H. Ziener, T. Kampf, G. Melkus, P. M. Jakob, and W. R. Bauer, J. Magn. Reson. **184**, 169 (2007).
[24] R. P. Kennan, J. Zhong, and J. C. Gore, Magn. Reson. Med. **31**, 9 (1994).
[25] T. G. Reese, R. M. Weisskoff, R. N. Smith, B. R. Rosen, R. E. Dinsmore, and V. J. Wedeen, Magn. Reson. Med. **34**, 786 (1995).
[26] S. B. Reeder, A. Z. Faranesh, J. L. Boxerman, and E. R. McVeigh, Magn. Reson. Med. **39**, 988 (1998).
[27] C. H. Ziener, S. Glutsch, P. M. Jakob, and W. R. Bauer, Phys. Rev. E **80**, 046701 (2009).
[28] W. R. Bauer, C. H. Ziener, and P. M. Jakob, Phys. Rev. A **71**, 053412 (2005).